DAYLIGHT LASER RANGING OF SPACE DEBRIS WITH A GEODETIC LASER FROM THE SWISS OPTICAL GROUND STATION AND GEODYAMICS OBSERVATORY ZIMMERWALD: FIRST EXPERIENCES

Julian Rodriguez-Villamizar and Thomas Schildknecht

Astronomical Institute University of Bern (AIUB), Sidlerstrasse 5, 3012 Bern , Switzerland, Email:
julian.rodriguez@aiub.unibe.ch

ABSTRACT

The Swiss Optical Ground Station and Geodynamics Observatory Zimmerwald (SwissOGS), operated by the University of Bern, Switzerland, has extended its capabilities for enabling laser ranging measurements to space debris. Starting in 2012, the SwissOGS successfully participated in multistatic experiments with other European partners as a passive receiver of the diffusely reflected photons for a decommissioned satellite and a spent upper stage. Next, in 2016 laser ranges gathered for the decommissioned satellite ENVISAT were processed and analysed in order to understand and derive an attitude model and its evolution with respect to time.

Recent developments in hardware include the use of a tracking camera, for correcting the pointing of the telescope in real time, when using ephemerides with compromised accuracy. In particular for daylight observations, the tracking camera is equipped with additional spectral filters to block radiation coming from the background, in particular from the diffusely scattered solar photons and from the backscattered photons of the emitted laser pulses. The implementation of an iris on the focal plane of the receiver path allows to reduce the field of view up to a minimum of 10 arcseconds. Furthermore, a combination of a Fabry-Pérot and a narrowband filter is inserted in the optical path of the receiver to ensure that only photons in the narrow ranges of 532 ± 0.15 and 1064 ± 0.15 nm wavelengths, centered on the wavelengths of our laser, may pass onto the receiver.

The software used to control all laser observations was adapted to include a new group of targets namely `space debris`. Since the initial software design was done to comply with precise geodetic standards, we needed to extend certain modules in the digital real-time filter, to discriminate actual photons backscatterd by the target object from the background. Moreover, we did a careful selection of potential targets according to the minimum observable optical cross section as a function of altitude, minimum expected return flux on the receiver, attitude and reflectivity of the surfaces of the target.

We will present our very first experiences in the observation of space debris using a low-power geodetic laser, highlighting the successful observations from passes during daytime.

Keywords: Satellite Laser Raning (SLR), Space Debris, Daylight, Active Tracking.

1. INTRODUCTION

The uncontrolled growing number of resident space objects (RSO) threatens all space-based operations. Specifically, the lack of accurate and precise knowledge of the space debris population, and its evolution with respect to time, will not allow to comply with the latest mitigation strategies proposed by the The Inter-Agency Space Debris Coordination Committee. One of those regulations addresses explicitly the reduction of collision probability, which cannot occur unless the information-content of each RSO is regularly monitored and updated. Within this context, the observation of daylight passes contributes chiefly to:

- A larger number of observed passes, i.e. larger orbital arc, which contribute to better estimates of the target's orbital elements and therefore faster re-acquisitions of the target object from a network of stations.

- The observation of different attitude states of the object by single and multiple stations observing with passive- and active- optical systems. The latter is critical when deriving an attitude and attitude motion model of the target object.

- To mitigate the reduced nighttime observation windows during summer, which is critical for northern and southern mid- and high- latitude observatories.

One reason to explain why up to now daylight observations are not routinely implemented stems from the fact that the observing sensors, sensitive within the solar spectrum, are flooded chiefly with diffuse or direct solar photons. For the detection of reflected photons from the target object, a normalized signal-to-noise higher than 50%

becomes imperative. Within the current work we will derive estimates for the signal, the noise and their ratio with the final aim of strengthening this ratio by attenuating the impact of the noise. Both approaches were implemented at hardware and software level particularized for the Zimmerwald Laser and Astrometry Telescope (ZIMLAT) and laser ranging system at the Swiss Optical Ground Station and Geodynamics Observatory (SwissOGS), operated by the Astronomical Institute of the University of Bern, Switzerland.

2. FIRST OBSERVATIONS

The first observation sessions conducted at the SwissOGS date back to March 2020 after the successful implementation of the robust and efficient active tracking that compensates for ephemerides of compromised accuracy. In general, for the preparation of observation sessions, we need to select a suitable set of targets. The criteria used for this selection are the culmination of the pass over the station, the sunlit condition, the phase angle, the slant range, the cross section of the target and the angle between the line of sight and the station-Sun direction. Note that the last one is only used for daylight observations. In the following subsections we will guide the reader through the steps conducted at the SwissOGS for the observation of space debris. Finally, we will show a case study of an object that gave us the right motivation for enhancing our detection capabilities.

2.1. Target Selection

The first set of targets were selected using the public catalog of the 100 brightest objects available in Celestrak [9]. After the analysis of the minimum observable cross section, we can filter the previous catalog and select the best candidates according to the radar cross section and the shortest geometrical distance to the station. A sample of the resulting set of targets are shown in Figure 1. Note that Figure 1 includes objects that already reentered. Furthermore, the radar cross section is used for approximating the optical cross section. Complementary to the previous set of target objects, we also included targets that were object of interest in specific space debris observation campaigns, besides the known ones through experience gained by dedicated space debris SLR stations.

2.2. Software Developments

Once we have a suitable set of target identifiers, e.g. the NORAD number, we can retrieve latest generated ephemerides available e.g. in the form of Two Line Elements downloaded from Space-Track [10]. Once downloaded, the state vector is propagated according to the Simplified General Perturbation Theory 4 and Cartesian
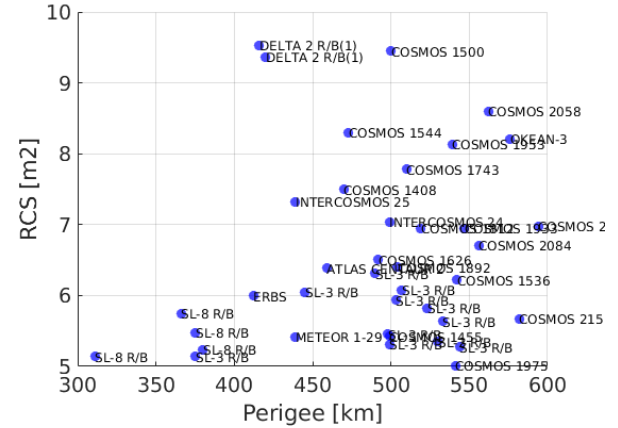

Figure 1. Distribution of target objects according to their radar cross section and perigee altitude. The information was retrieved from the public catalog of the 100 brightest objects available in Celestrak.

3D coordinates are computed in the International Terrestrial Reference Frame using the International Earth Rotation Service 2010 conventions. The used format is the Consolidated Prediction Format (CPF) specified by the International Laser Ranging Service (ILRS) [7]. The inclusion of the CPF's into our system is done via a pipeline written in Perl, which allocates a dedicated slot per target. Currently we can schedule up to 28 space debris targets, while the laser system is working in active mode, and up to 20 more different slots are utilized by the laser system for multistatic observations. Furthermore, information about the phase angle, horizontal and celestial coordinates, slant range and further available information such as the radar cross section, is retrieved and output in a separate file. The previous file is used to rank the different passes according to the chances of receiving backscattered target photons.

The observation of space debris are conducted as special observation sessions interrupting the highly automated working mode of ZIMLAT, which consists of regular satellite laser ranging observation to ILRS targets, astrometric and photometric observations. Note that the last two occur only during the nighttime.

2.3. Case Study NORAD 31114

The first observations of rocket bodies conducted at the SwissOGS, indicated that further modifications needed to be done in order to detect the target. The next example shows a pass observed on June 12, 2020, at 19:30 UTC when the Sun was still above the horizon. This particular spent upper stage has been cataloged as a potential pseudo-cooperative target since regular SLR stations have been able to observe it. Nonetheless, as shown in Figure 2 our real-time SLR filter was not able to discriminate the signal of the target object. Each single point-like feature in Figure 2 indicates a triggered photoelectron on the receiver, which was represented using a transparency

of 75% in order to aid the reader to see the actual signal's trace. In Figure 2 we can see that despite widening the range gate up to 8 μs, we can barely see the object until the last portion of the pass. Close to 19.65 hour, we recognized visually the target and reduced the range gate to nudge the filter, but was not successful. The main reason for the failure stems from the fact that the observed-minus-computed feature shows a significant slope and by our current geodetic parametrization of the filter, the discriminator was not able to find sufficient close returns to be able to track the object. Note that in Figure 2 one does not appreciate the steepness of the signature due to the scaling of the range gate and the total length of the observed pass. The previous example and others gave us
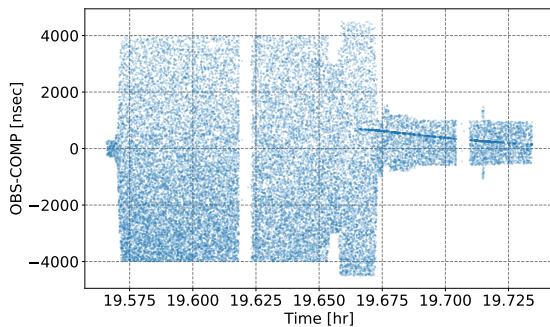

Figure 2. Example of laser ranging observations during a daylight pass of a rocket body, presumably a pseudo-cooperative, on June 12, 2020, at 19:30 UTC. Each single point-like feature indicates a photoelectron triggered at the receiver represented using a transparency of 75% to aid the reader in the visualization of the signal's trace. The y axis indicates the observed minus predicted values using the predictions generated by the latest TLE.

the right motivation to enhance our detection capabilities for adapting to the new challenging paradigm.

3. THE SLR REAL-TIME FILTER

The satellite laser ranging real-time filter is a special feature of the laser raging system at the SwissOGS. Its main parameters were adapted through more than 30 years in order to enhance the performance of the complete system tailored specifically per each single target. Next, we will present the main characteristics of the algorithms highlighting the necessary changes and adaptations for the special observation of space debris.

3.1. Filter Algorithm

In Figure 3 we show the main structure of the algorithm, conveniently divided into two blocks: initialization and tracking blocks at the right and left side of the flowchart in Figure 3 respectively.

The SLR filter consists of the orbit improvement of only one orbital element: the perigee passing time. The estimation of the perigee passing time makes use of the variational equations, i.e. how much does the range change due to a variation in the perigee passing time. For the implementation, the algorithm requires the specification of an initialization file and the corresponding predictions associated to the target object of interest. The two main critical parameters for the detection are the length of the observation window and the target depth. The length of the observation window is defined by a minimum number of n entries. Additionally, the standard deviation of the range measurement σ_0, which in the case of space debris is dominated by the target depth, was optimized for each target object. Despite of being defined in the initialization file, the previous parameters can be modified in real-time by the observer.

During the initialization phase, observations start accumulating until fulfilling the minimum number of n entries. Note that the first condition filters out all outgoing pulses, using a repetition rate of 100 Hz, for which there was not an expected return and therefore are assumed to be noise. Next, per each actual measurement, the exact time-of-flight, its first and second derivatives are computed. Once the derivatives are available, the value σ_{init1} is calculated, which will be needed further on. Thereupon, the observed minus computed term OmC is calculated and the variational equation for the perigee passing time $\Delta DT0$ is solved [8]. For the n entries we compare separately how close the terms $\Delta DT0$ and OmC are with respect to the defined threshold, and apply a majority voting step using first the dynamical information, i.e. $\Delta DT0$, or the geometrical information, i.e. OmC. Note that the latter is the conventional histogram-based approach.

Once the initialization is successful, we shift into the tracking block. The tracking block was implemented as a Kalman Filter, where the unique updated parameter is the solution for the variational equation of the perigee passing time. In addition, the remaining trend between observed minus computed is removed estimating it as the range bias. With the updated orbit we re-estimate the OmC term and compare it against a tolerance specified for the tracking filter σ_{tol}, which may, or not, coincide with the one defined at the beginning σ_0. If the test fails for the incoming measurement, a certain time interval Tol_{time} is specified comparing the elapsed time between the last successful observation and the most recent one, setting the initialization flag to none in case the condition is not satisfied. On the other hand, if the measurements were successful, we mark them as good ones by the real-time filter (RTF) and add the next measurement. The latter flag is crucial for further post-processing steps. It is important to notice that once the initialization flag is set, the system in the background reduces the size of the range gate from RG_{ini} to RG_{tra} in order to increase the signal-to-noise ratio (see Table 1).

In Table 1 we show a comparison between standard values within the initialization file for the geodetic and the new space debris categories. Note that we show only the values associated to daylight observation since, within the initialization file, we can also define parameters for night-
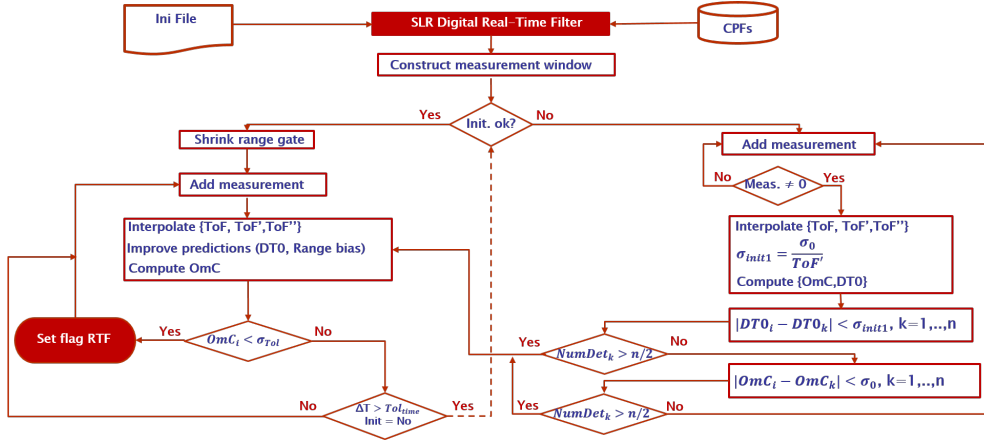
Figure 3. Schematic of the satellite laser ranging real-time filter at the SwissOGS. The right block corresponds to the initialization part of the algorithm while the left corresponds to the tracking.

time observation. The target depth expected for a space debris object is in the order of the meter, while for geodetic standards could be smaller by even two order of magnitudes. In addition, the width of the range gate RG is a function of the quality of the predictions, thus significantly shorter for geodetic targets.

Table 1. Set up of real-time SLR filter parameters for geodetic and space debris categories.

	Geodetic	Debris
σ_0 [nsec]	0.2	3
σ_{tol} [nsec]	0.4	3
n	20	20
RG_{ini} [μs]	0.6	1
RG_{tra} [μs]	0.04	0.1

It should be noted that all the previous parameters might be modified interactively by the observer when performing regular or special sessions. We take special advantage of this feature to reduce the range gate at the time of closest approach in order to maximize the chances to get backscattered photons from the object of interest.

3.2. Re-Processing NORAD 31114

To validate the improvements in the real-time filter we post-processed, once again, the case that failed with the normal set up for the spent upper stage with NORAD number 31114. In Figure 4, each point-like feature was represented without transparency, but color coded representing the signal and the noise. Despite the high density of photoelectrons within the OmC space, Figure 4 shows the successful detection of the previously undetected signal. Several more cases were re-processed and the results did show an actual improvement. Further developments at the SwissOGS are currently on-going to implement off-line data processing schemes for the raw

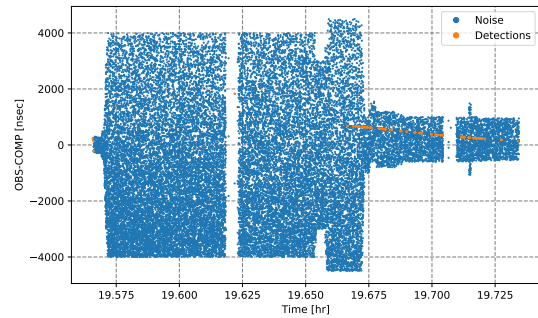data processing of satellite laser ranging measurements to space debris.

Figure 4. Re-processed upper stage pass with NORAD number 31114 observed on June 12, 2020, at 19:30 UTC. The color code is used to represent the signal and the noise. The detected signal matches with the clear undetected signal's trace visible from the original acquisition using a transparency of 75% (see Figure 2).

4. CASE STUDIES

In this section we present selected cases of passes that were successful after the adaptation and enhancement of the satellite laser ranging system at the SwissOGS. Back in 2016, we were limited to observe only pseudo-cooperative targets, in particular the decommissioned target ENVISAT, using CPF's generated by different prediction centers of the ILRS. Our capabilities were extended to observe objects using TLE ephemerides and correcting the offset with respect to the true position of the object in the sky, by using a tracking camera and sophisticated image processing and tracking components. As a result, today we are operating a combined passive- and active optical system, which allow us to retrieve laser ranges, pointing direction, i.e. azimuth and elevation, and ap-

parent brightness; all of them simultaneously and in real time. Note that the last one is a by-product of the object recognition phase within the image processing component.

4.1. Observation of NORAD 11327

According to the information provided by DISCOS [11], the target object is a second stage cylindrical rocket body, with a maximum cross section of 16.4 m^2 and mass of 1421.21 kg and is presumably a non-cooperative target. The date of observation was on June 24, 2020, at 18:36 UTC when the Sun was at 7.85° above the local horizon. The observed passed is shown in Figure 5.
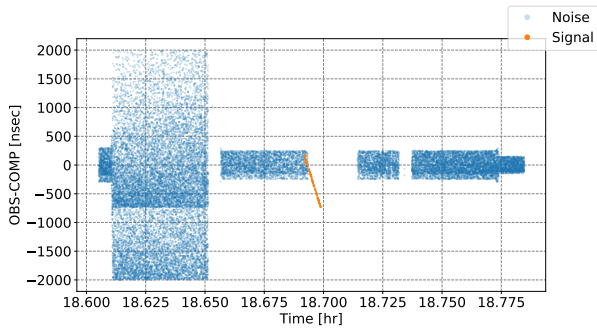

Figure 5. Laser ranging observations to the target with NORAD id 11327 on June 24, 2020, at 18:36 UTC. The signal corresponds to detection events at the time of closest approach with respect to the observing station. The remaining portion of the pass was left to test for potential false positives. The gaps during the pass correspond to air traffic safety measures. Transparency of 50% was applied in each single triggered photoelectron to aid in the visualization of the results.

The target culminated at an elevation of 76° over the SwissOGS. From the total pass we were able to get 73 good measurements after detection. During the observation of this pass we first tried to widen the range gate to search for the target. Since we were not successful we decided to shorten the range gate near the time of closest approach, where we were expecting a zero crossing in the OmC component. The zero crossing event occurs as a consequence of the symmetrical observation of the pass with respect to the culmination (assuming that the prediction error is mostly an along-track offset). As an example, if the predictions are behind the true position of the object in the sky, the difference OmC will be negative, while after the culmination the difference will be positive. Additionally, to ensure that the measurements were real, we left the range gate at the same width for the remaining portion of the pass, even shortening it a little at the very end, to reduce the possibility of potential false positives. The detection of signal after the time of closest approach, orange trace, will questioned the reliability of the first detection. By computing the histogram using the data shown in Figure 5, we confirmed how the number

of background photoelectrons increased while observing the pass since we were reducing the angular distance between station-target and station-Sun. The gaps in the pass correspond to air traffic safety measures.

4.2. Observation of NORAD 28480

The next target object of interest is the cylindrical rocket body with NORAD id 28480. The maximum cross section of the object is 29 m^2 with a mass of 3800 kg [11]. The target object has presumably more than one highly reflective element compared to the reflectivity of the main body. The next pass was observed on August 15 2020 at 18:47 UTC. In Figure 6 we show the detection occurring near the time of closest approach to the station. The detected signal depicts a noticeable slope caused mainly due to the quality of the predictions. From the observed pass we were able to retrieve 157 good measurements after detection. Despite of being able to retrieve measurements within few seconds only, we were able to estimate a single pass constraint-less orbit improvement. The residuals after the orbit improvement are shown in Figure 7. The residuals depict a rather interesting feature. The recognizable trace at the bottom in Figure 7, shows the attitude behavior of presumably one of the highly reflective elements of the rocket body, suggesting even a periodicity. On the other hand, the upper trace depicts a sparse feature, which might potentially come either from diffuse reflections from other highly reflective surface, pre- or post- pulses in the laser system, or from the non highly reflective part of the rocket body. To further understand the results, we studied each possibility separately.
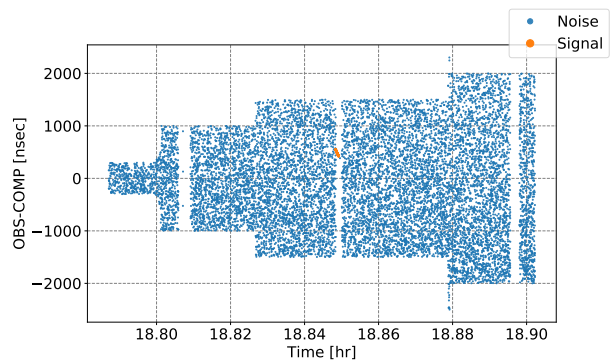

Figure 6. Laser ranging observations to the target with NORAD id 28480 during daylight. The signal detection occurs next to the time of closest approach to the observing station with a significant slope stemming from the quality of the predictions. The 157 measurements were used for a single pass constraint-less orbit determination.
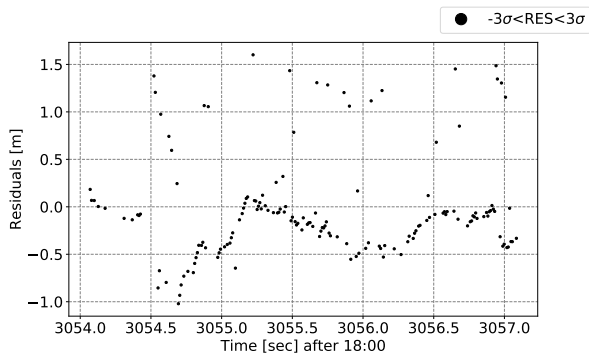
Figure 7. One way single pass residuals after a constraint-less orbit improvement using measurements acquired during daylight.

– Pre- or post- pulses. To exclude the presence of either event, we monitored the triggered signal at the start diode with the aid of an oscilloscope (see Figure 8). From the experiment, we could see that chiefly the pre-pulses were a multiple number of the laser cavity length. The exclusion of the post-pulses is more challenging due to its dependency on the signal's intensity variation. After extensive experimentation, we took representative values of the highest two main post-pulses.
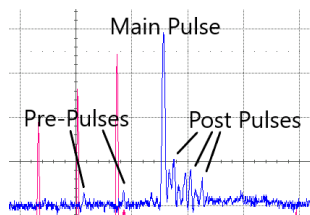

Figure 8. Example of pre- and post- pulses monitored by the oscilloscope. Each division represents 20 nsec.

After the previous analysis we could exclude this possibility, but not without knowing that slight variations on the signal could produce changes in the behavior of the post-pulses. In future experiments, the observation of a longer arc could definitely help to clarify the behavior of the sparse trend if stemming from this effect.

– Diffuse reflection from another reflective element. The lack of knowledge with respect to the type of reflective element, or the few of them, and distribution on the rocket body and alignment, with respect to the laser beam, poses an ambiguity that is not easy to solve. Here the synergy between passive- and active- optical systems, over several passes, will potentially improve our knowledge of the target object.

– Diffuse reflection from body. This possibility exists due to mainly the large cross section of the target and the increase in gain after selecting a suitable beam

divergence and correcting the pointing of the telescope using a passive optical system. The estimated return rate using the link equation is in agreement with the observed one. The reliability on the link equation stems from its validation using one year observations to the well-known LAGEOS-1 target.

Due to all the unanswered questions the object with NORAD id 28480 is of particular interest to us. Next, we will present the 4-dimensional real-time measurement capabilities of the satellite laser ranging system at the SwissOGS, from which we were able to infer the presence of more than one highly reflective element in the rocket body, without the use of a kilohertz laser ranging system. The observation of the next pass was conducted on July 8, 2020, at 19:33 UTC. In this occasion the target culminated at an elevation of $31°$. From the observed pass we retrieved 819 good observations, which were used for a single pass constraint-less orbit improvement. The residuals after the orbit improvement are shown in Figure 9.
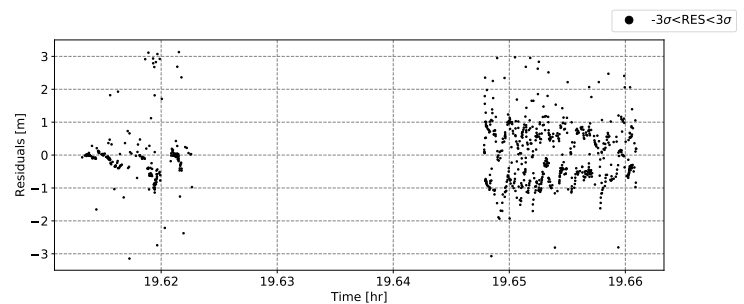

Figure 9. One way single pass residuals after a constraint-less orbit determination.

To acquire ranges, the target object was followed by the telescope using a tracking camera processing real-time acquired images and correcting the pointing of the telescope as soon as the target was detected. Once detected, the estimated differential corrections on the camera reference system were transformed into horizontal offsets, i.e. differential corrections in azimuth and elevation. A byproduct of the object recognition procedure is the apparent brightness of the target object. The latter is used complementary to the previously acquired ranges and horizontal angular values azimuth and elevation. The acquired changes in brightness by the real-time procedure are shown in Figure 10. The main trend of the extracted light curve is dominated by geometrical components, i.e. distance station-target and phase angle. The dispersion of the brightness indicate a rather low contrast between the sky background and source. Despite the influence of the observing conditions on the apparent brightness, the extracted light curve depicts critical points matching with the returns acquired with the laser ranging system. Those correlations complement each other and aid in the understanding of the attitude, attitude motion, number of reflecting elements and location of the reflecting elements withing the rocket body.
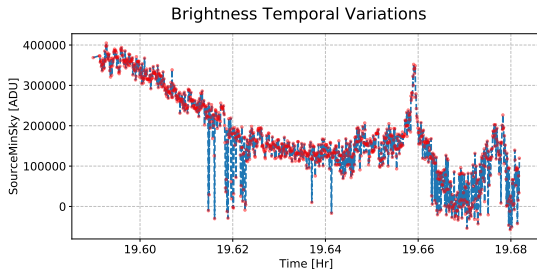
Figure 10. Variations in apparent brightness as derived from the real-time object recognition procedure implemented at the SwissOGS. The dispersion of the measurements occurs as a consequence of the low contrast between the sky background and source. The temporal changes in brightness add one observable more to the existing set of ranges, azimuth and elevation.

For the remaining analysis, we will divide it into two parts: the first around 19.62 hour and the second between 19.65 and 19.66 hour.

– First part. From the one way range residuals, we see that from this portion of the pass we got higher return rates, which could come from a highly reflective element probably aligned favorably with respect to the laser beam. Note that the number of return rates coming from each reflecting element will weight differently in the the single pass orbit improvement solution using ranges only, meaning that the zero mean residual might not correspond necessarily to the center of mass of the satellite. After the first detection, the trend due to the attitude motion of the target becomes apparent. In addition, once again we see a sparse photoelectron trace centered around 3 m. The latter might suggest the exclusion of after pulses due to strong backscattered photons; see, e.g. the beginning of the detections were there is a high concentration of photoelectrons around 0 m but there is no second trace. From the light curve, we do not see a special feature that might correlate with the behavior depicted by the range measurements. We can see nonetheless, a significant number of outliers indicating that the signal-to-noise ratio between source and background was compromised. Bear in mind the observation conditions.

– Second part. From the changes in brightness we see a clear maximum indicating potentially the observation of the largest cross section of the target, a favorable phase angle given by the attitude state of the target and its Sun-Earth configuration at that specific epoch, or a combination of both. From the one way range residuals, we can identify at least two highly reflecting elements with an initial separation of 2 m narrowing up to 1 m, which could be addressed to changes in the attitude state. One likely explanation is that at the beginning of the complete pass we were observing only one reflective element from where we got the highest density of measurements,

therefore biasing the estimated orbit around them. Due to its attitude and attitude motion, the first reflective element changed its position with respect to its previous one and a second reflective element was unveiled from the rocket body surface with respect to the laser beam. The previous statement is justified by seeing the distribution of the residuals coming from the beginning of the pass. However, there is also the possibility of seeing two new highly reflecting elements. In this regard, the collection and fusion of measurements of different nature, different observation geometry, and at different and simultaneous acquisition times is of paramount importance. Finally, the presence of a third trace suggests the presence of either diffuse reflections from a highly reflective element or contributions from the remaining irradiated part of the rocket body. The general trend of the sparse string of photoelectrons correlates with the behavior given by the two identified highly reflective elements.

5. SUMMARY

Daylight observations are a valuable asset for a Space Surveillance and Tracking system due to mainly the possibility to observe more passes. The latter not only means the observation of a larger orbital arc, but the observation of different attitude states, under different aspect angles and illumination conditions, that might help in the derivation of an attitude model and its variation with respect to time. Through the current work we were able to:

– Enhanced our detection capabilities. By the modification of the existing software within the laser ranging system, we were able to find signal were the previous real-time SLR filter failed.

– Showed successful cases of daylight observation of space debris demonstrating a 4-dimensional observation capability. Furthermore, we could process very-short arcs in a single pass constraint-less orbit determination. An analysis of the observed passes was done in an attempt to further understand the attitude and attitude motion of the target object.

– Analyzed the target with NORAD 28480 and derive plausible hypothesis for its attitude state, and attitude motion, with the aid of laser ranges residuals, after a constraint-less orbit determination, and the light curve. From the laser ranging measurements we were able to discern the contribution from more than one highly reflective element, which occurred at an epoch where the light curve depicted a local maxima. The synergy between the two optical techniques highlights the importance of merging data coming from more than one measurement type.

ACKNOWLEDGMENTS

REFERENCES

1. Zdunkowski, W., Trautmann, T., & Bott, A. (2007). *Radiation in the atmosphere: a course in theoretical meteorology*, Cambridge University Press

2. Kneizys, F. X., Shettle, E. P., Gallery, W. O., Chetwynd Jr, J. H., & Abreu, L. W. (1983). Atmospheric transmittance/radiance: computer code LOWTRAN 6. Supplement: Program listings. Air Force Geophysics Laboratory, United States Air Force.

3. Kneizys, F. X. (1988). Users guide to LOWTRAN 7 (No. 1010). Air Force Geophysics Laboratory, United States Air Force.

4. Coddington, O., Lean, J. L., Pilewskie, P., Snow, M., Lindholm, D. (22 August 2016). *A Solar Irradiance Climate Data Record*, Bulletin of the American Meteorological Society. 97 (7): 12651282.

5. Steindorfer, M. A., Kirchner, G., Koidl, F., Wang, P., & Kucharski, D. (2019). Recent Space Debris Related Activities at the SLR Station Graz, *Proceedings NEO and Debris Detection Conference, Darmstadt, Germany*

6. Klein, B. J., & Degnan, J. J. (1974). Optical antenna gain. 1: Transmitting antennas. *Applied optics, 13(9)*, 2134-2141.

7. Pearlman, M. R., Degnan, J. J., & Bosworth, J. M. (2002). The international laser ranging service. *Advances in Space Research*, 30(2), 135-143.

8. Beutler, G. (2005). *Methods of Celestial Mechanics: Volume I: Physical, Mathematical, and Numerical Principles.* Springer Science & Business Media.

9. Celestrak. *https://celestrak.com/NORAD/elements/.* Accessed on February 28 2021.

10. Space-Track. *https://www.space-track.org/.* Accessed on March 1 2021.

11. DISCOS. *https://discosweb.esoc.esa.int/.* Accessed on March 1 2021.